Artifical compound eyes – different concepts and their application to ultra flat image acquisition sensors

Jacques Duparré[a], Peter Schreiber[a], Peter Dannberg[a], Toralf Scharf[b], Petri Pelli[b], Reinhard Völkel[c], Hans-Peter Herzig[b], Andreas Bräuer[a]

[a]Fraunhofer–Institut für Angewandte Optik und Feinmechanik, Albert-Einstein-Str. 7, D-07745 Jena, Germany
[b] University of Neuchâtel, Rue A.-L. Breguet 2, CH-2000 Neuchâtel, Switzerland
[c]SUSS MicroOptics SA, Jaquet-Droz 7, CH-2007 Neuchâtel, Switzerland

ABSTRACT

Two different approaches for ultra flat image acquisition sensors on the basis of artificial compound eyes are examined. In apposition optics the image reconstruction is based on moiré– or static sampling while the superposition eye approach produces an overall image. Both types of sensors are compared with respect to theoretical limitations of resolution, sensitivity and system thickness. Explicit design rules are given. A paraxial 3x3 matrix formalism is used to describe the arrangement of three microlens arrays with different pitches to find first order parameters of artificial superposition eyes. The model is validated by analysis of the system with raytracing software. Measurements of focal length of anamorphic reflow lenses, which are key components of the superposition approach, under oblique incidence are performed. For the second approach, the artificial apposition eye, a first demonstrator system is presented. The monolithic device consists of a UV–replicated reflow microlens array on a thin silica–substrate with a pinhole array in a metal layer on the backside. The pitch of the pinholes differs from the lens array pitch to enable an individual viewing angle for each channel. Imaged test patterns are presented and measurements of the angular sensitivity function are compared to calculations using commercial raytracing software.

Keywords: Compact digital camera, insect vision, compound eyes, vision systems, microlens arrays, micro–optics, paraxial matrix optics, anamorphic lenses

1. INTRODUCTION

Recent improvements of CMOS image sensors would allow a further miniaturization of digital micro–cameras. However, due to diffraction effects, a simple miniaturization of known classical imaging optics would drastically reduce resolution and image finesse or field of view (FOV).[1] How to overcome these limitations of optics? A fascinating approach is to look how mother nature has successfully solved similar problems in the case of very small creatures.[2]

There exist two known types of animal eyes[3]: Single aperture eyes and compound eyes which can be divided into apposition compound eyes and superposition compound eyes (Fig. 1). All of theses eye types can use refractive and reflective mechanisms for image formation. Single lens eyes served as antetypes for classical single aperture objectives. Assets of single aperture eyes are sensitivity and resolution while overall FOV and volume are drawbacks. The behavior of those classical optics is today well understood.

Apposition eyes consist of an array of lenses and photo receptors. Each lenslet focuses light from a small solid angle $\Delta\phi$ of object space onto a single photoreceptor (See Fig. 1). The single lens–photoreceptor system is referred to as ommatidium. Apposition eyes have some hundreds up to tens of thousands of these ommatidia packed in non–uniform hexagonal arrays, which sample the angular object space with the interommatidial angle $\Delta\Phi$. The

Further author information: (Send correspondence to Jacques Duparré)
Jacques Duparré: E-mail: jacques.duparre@iof.fraunhofer.de, Telephone: +49 3641 807380
Toralf Scharf: E-mail: toralf.scharf@unine.ch, Telephone: +41 32 7183286
Reinhard Völkel: E-mail: voelkel@suss.ch, Telephone: +41 32 7205103

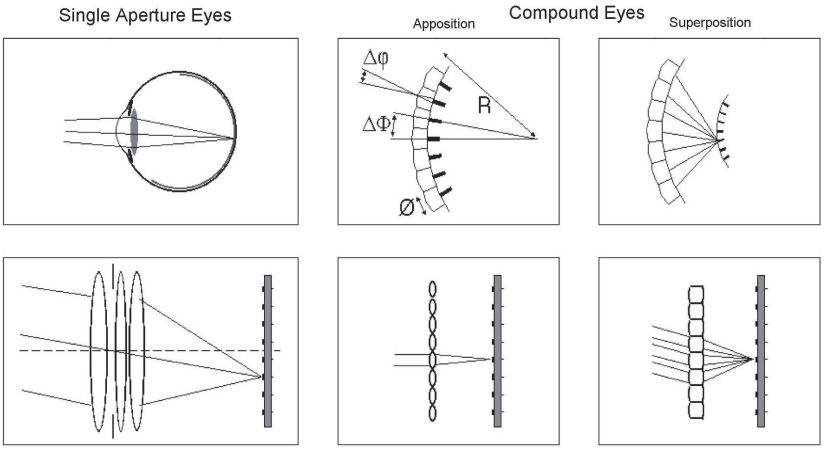

Figure 1. Different types of natural eye sensors and their technical counterparts.[2] Problems occur if natural concepts of eyes where optical surfaces and receptor arrays are situated on curved surfaces have to be transferred to technical solutions where lens arrays or receptor arrays are usually only available on flat surfaces.

FOV of such an imaging system is determined by the radius of curvature R and size of the eye. The acuity of natural compound eyes was examined by many authors.[4–8] It was found, that apposition compound eyes have low volume and a large FOV but this is paid by low spatial resolution and sometimes low sensitivity.[9,10] They often work close to the diffraction limit. Different types of miniaturized artificial apposition compound eyes were examined.[11–13] To our knowledge, the described technological approaches suffer from assembly misalignment errors of the components which could be avoided by using micro–optical fabrication– and assembly technologies utilizing lithographic accuracy.

The superposition compound eye has primarily evolved on nocturnal insects and deep–water crustaceans. The light from multiple facets combines on the surface of the photoreceptor layer to form a single, erect image of the object. Compared to apposition eyes, the superposition eye is much more light sensitive, but spherical aberrations caused by the combination of light from many facets lead to a resolution far from the diffraction limit.[3,14] The technical equivalent of the superposition eye is the Gabor–Superlens.[15,16]

Due to small necessary lens sags artificial compound eyes are well suited for micro–optical fabrication technologies which allow wafer level manufacturing with lithographic accuracy. In the following, we want to give an overview of two different concepts based on artificial compound eyes we pursuit.

2. CLUSTER EYE

Figure 2 presents an imaging system with vanishing overlap of the images transferred by different channels. A perfect spatial annexation of the individual sub–images leads to the upright overall image in the detector surface. Three microlens arrays (MLA) with different pitches form Keplerian telescopes including a field lens– and field aperture–array in the intermediate image plane. The system is a cluster of single pupil micro–cameras which have tilted optical axes to obtain a large overall FOV.[17] Each channel images only a small angular section. The aperture sizes of the field stop array determine the amount of overlap of the micro images. Due to the arrangement of the refracting surfaces the proposed system operates like a superposition eye. Due to the implementation of a field aperture array to some extend it also works like an apposition eye. We want to call it cluster eye. If the field stop array is removed the system acts as a Gabor–Superlens (Fig. 3 (b)).

2.1. Design

Because of the large number of parameters coupled with each other, the cluster eye possesses a very large solution space. We used a paraxial 3x3 matrix–formalism[18,19] which accounts for lens decentrations to find the first order parameters of the system. A number of different conditions have to be fulfilled to guarantee the desired optical

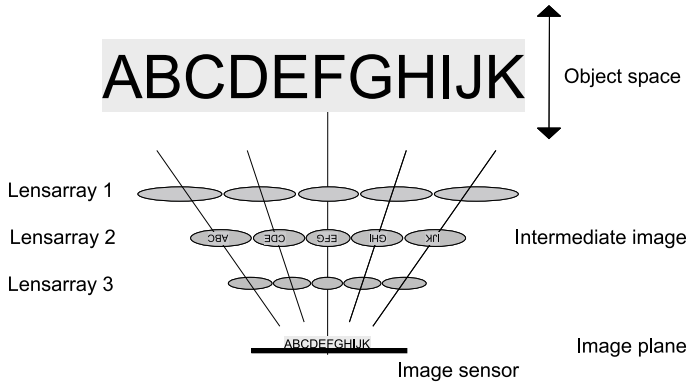

Figure 2. Working principle of the described compound–eye–type imaging system with optical image reconstruction.

Table 1. Parameters of example systems presented in raytracing simulations.

Parameter	**Paraxial example**	**Real lenses with toric lenses**
$F/\#$	2	10
Overall length	2mm	1.96 mm
FOV (full angle)	70 deg x 15 deg	90 deg x 10 deg
Detector width	4.5 mm	4.5 mm x 0.5 mm
Number of channels	column of 5	vertical: 25 horizontal: 3

performance. This leads to an equation system where all desired optical system parameters like FOV, detector size, $F/\#$ and length are coupled to the geometrical parameters such as focal lengths, pitches and axial spacings of the individual lenslets. By solving this equation system for the geometrical parameters we obtain another equation system which describes the geometrical parameters as a function of the optical system parameters. A more detailed description of the design strategy of the presented cluster eye is given in.[20] For demonstration purposes the paraxial geometrical parameter sets obtained by these formulas are implemented with paraxial lens models into raytracing software. In Fig. 3 (a) a system with a column of five channels is shown (parameters in Table 1). Each channel transmits a portion of the overall FOV which is controlled by the spectrum of input angles for each individual channel to avoid spurious light or crosstalk. In a "real" system field stops in the plane of the intermediate image will determine the individual FOV and additional baffles in different surfaces will block the spurious light. The maximum marginal field of one channel is the minimum marginal field of the adjacent channel. A perfect annexation of the individual sub–images to one overall image can be noticed. Figure 3 (b) demonstrates the behavior of the described system operating as a Gabor–Superlens where all channels contribute to the image point for a given angle of incidence if no constraints for the individual FOVs are given.

The calculated paraxial geometrical parameters are used as starting values for a system consisting of real MLA–telescopes. When transferring the paraxial parameters to the parameters of real lenses the focal lengths and apertures have to be a function of the main field angles (tilt of the optical axis) of the considered channel in order to minimize the off–axis aberrations, especially astigmatism and field curvature and to keep the light flux through the projected aperture constant, respectively. Anamorphic lenses with different radii of curvature and lens sizes as a function of the channel number are established. From raytracing simulations and third order aberration theory it follows that the focal lengths of the lenses must change with $1/\cos^2(\theta)$ in direction where the field angle θ is increased (y–direction) and with $1/\cos\theta$ in the perpendicular (x–) direction in order to keep the image surface of each channel at the position of the detector surface. To maintain the light flux independently from field angle, the lens aperture in y–direction has to change with $1/\cos\theta$.

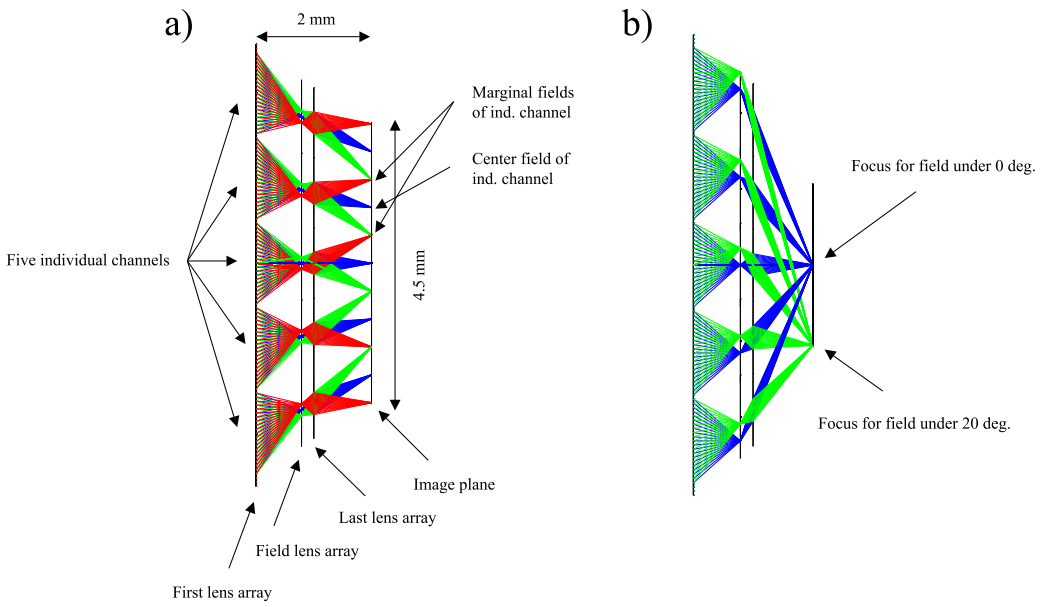

Figure 3. Paraxial five–channel example system for demonstration of the image transfer principle (a). Demonstration of the behavior like a Gabor–Superlens (b).

For validation of the paraxial design strategy and the recipe for the channel dependent transfer of the paraxial lens parameters to toric lenses, we simulated a system described in Table 1. For this set of parameters we obtained reasonable numerical apertures (NA) of the microlenses. The simulation results for wavelength 550 nm and lenses with spherical curvatures are presented in Figures 4 and 5. We optimized the lens curvatures in x– and y–direction as well as lens positions to obtain minimum spot size and good image annexation. Using anamorphic lenses we can minimize astigmatism and field curvature to large extend but coma is still present. Over the entire FOV only a small increase of the geometrical spot size can be observed. The magnification is nearly constant for all channels and we observe a perfect alignment of the sub–images to one overall image. However, due to the large individual channel $F/\#$s the airy disk diameter of the two presented systems are in in the magnitude of 10 to 15 μm and sensitivity is reduced. However, the presented simulations demonstrate that the idea of the separate partial image transfer and image reconstruction by annexation of the sub–images works very well.

The sensitivity of an imaging system to an extended source is determined by the system $F/\#$.[6] The sensitivity is proportional to $\sin^2(u)/m^2 = \sin^2(\acute{u}) = 1/(4F/\#^2)$ where $\sin(u)$ and $\sin(\acute{u})$ are the NAs in object space and in image space and m is the magnification of the optical system.[21,22] Technological constraints and aberrations limit the NA of the microlenses to a maximum of about 0.3 – 0.4. With this constraint minimum achievable individual channel $F/\#$s are calculated as a function of system length for all other optical parameters fixed as above (Fig. 6). For fixed magnification and fixed NA of the microlenses the individual channel $F/\#$ increases with decreasing system length because of stronger segmentation of the cluster eye.

The arrangement of toric lenses presented above makes use of lenses with maximum NA of 0.2 in order to reduce aberrations. Thus the system is situated above the presented curve in Fig. 6. We can draw the following conclusion:

- A low segmentation (small number of channels) is desired in order to achieve a low $F/\#$. This results in high sensitivity and small diffraction limited spots.
- For short systems small segmentation leads to large aberrations.

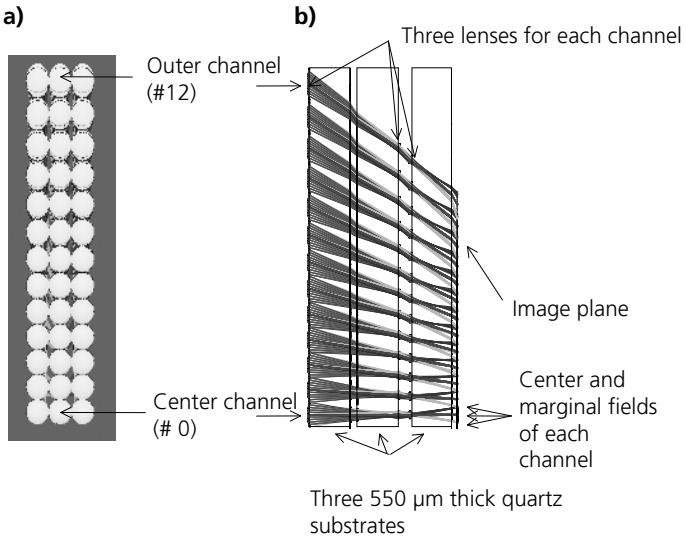

Figure 4. Cluster eye in a rectangular arrangement of toric lenses in a matrix of 25x3 channels. Only channels 0 to 12 are shown due to the y–symmetry of the system. (a): Front view of the system showing the increasing elipticity of the lenses with increasing field angle. (b): Side view of the system. Three toric lens arrays are placed on 550 μm thick quartz substrates. For each channel the central field as well as the y–marginal fields are shown. A perfect annexation of the individual sub–images to one overall image can be noticed.

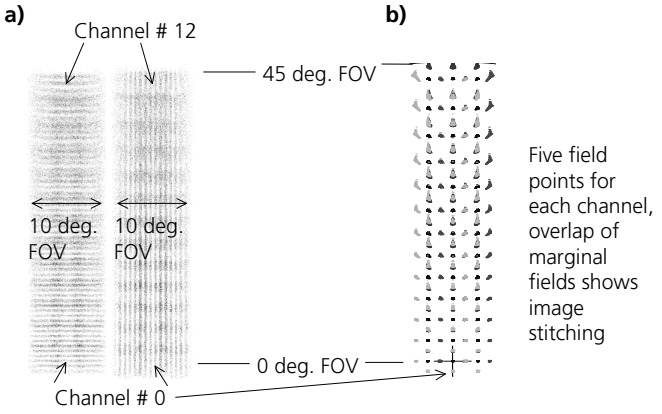

Figure 5. Analysis of system presented in Fig. 4. Only field angles from - 1.8 to 45 deg are shown due to y–symmetry. (a): Horizontal and vertical sample objects with 1.2 LP/deg are imaged by the cluster eye. The resolution of the patterns decreases with increasing y–field angle due to aberrations and image overlap. However, even for large field angles the line patterns can be resolved (b): Spot diagram of the presented system. For each channel a central and 4 marginal field bundles (+x,-x,+y,-y) are traced. The maximum marginal field of one channel is the minimum marginal field of the adjacent channel. Increasing spot size with y–field due to coma as well as very good overlap of marginal fields of adjacent channels can be observed.

- An optimum between the three contradictious requirements length, channel number (corresponding to the inverse of the channel $F/\#$.) and lens NA (corresponding to aberrations) has to be found.

We see that the potential shortness and large FOV of cluster eye systems have to be paid by a reduction of resolution and sensitivity.

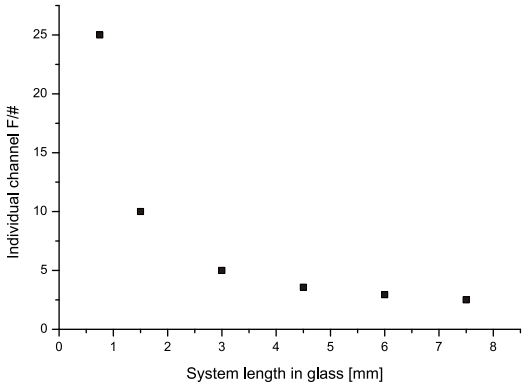

Figure 6. Individual channel $F/\#$ vs. system length for maximum lens NAs of 0.3-0.4 in case of no image overlap.

2.2. Fabrication and Testing of Anamorphic Lenses

As presented in the previous section anamorphic lenses are required in the cluster eye to correct for astigmatism due to oblique incidence. In order to be able to fabricate exactly the desired anamorphic lenses for the different channels of the cluster eye a realistic model fit of elliptical lenses fabricated by reflow process and subsequent RIE into silica is undertaken.

The elliptical lenses were inspected by microscopy and characterized with a Mach–Zehnder interferometer for radius of curvature– and Strehl–ratio– measurements and an Alpha–Step profilometer for lens height determination. To model the reflow process of elliptical lenses Lindlein N. et al. have derived equations to simulate such lenses considering a general ellipsoid.[23] Starting from a photoresist cylinder with an elliptical rim an elliptical lens is formed after melting and the parameters of the general ellipsoid are determined by taking into account volume conservation, fixed resist boundaries and surface tension. The model allows to determine relations between base ellipse semi–diameters and radius of curvatures of melted microlenses. We will refer to this model as the Lindlein–model. A result of this model is that the ratio between radius of curvature in x–direction R_x and radius of curvature in y–direction R_y can be assumed to be proportional to the square of the ratio between the semi–diameters a_x and a_y

$$\frac{R_x}{R_y} = \frac{a_x^2}{a_y^2}. \tag{1}$$

These ratios are plotted in Fig. 7 a) for different elliptical lenses. The semi–diameters a_x and a_y are varying from 250 to 350 μm. The largest deviation of the measured values from this equation is 3.8%.

Equation 1 implies that if one semi–diameter is fixed and the other is varied the lens height and therefore the radius of curvature in the fixed axis will be constant. To proof this we measured the lens height and radius of curvature for elliptical lenses with different ellipticity. Fig. 7 b) shows that in case of elliptical lenses if only one semi–diameter is changed the radius of curvature of the corresponding axis remains constant within the measurement errors.

Closer inspection of the results shows that there is a certain validity range of the model. For low numerical–aperture–lenses the radius of curvature corresponding to the long axis will not follow anymore the proposed law. To examine these limitations we measured the radii of curvature and lens heights and compared the results to the Lindlein–model. As an example the lens height measurements are shown in Fig. 8.

It can be seen that the measured heights differ quite remarkable form the model calculation. In the Lindlein–model the volume is supposed to be constant, but in reality a volume loss is probable. There are at least two reasons which cause volume loss. One is material evaporation during melting and another is caused by some unexposed resist removing during development. For spherical lenses (lens diameter 250 μm) this loss was about 17 % for our lens fabrication technique. Due to this effect one has to make a correction when approximating lens parameters with the Lindlein–model. In Fig. 8 the result of the model calculation with the corrected volume is

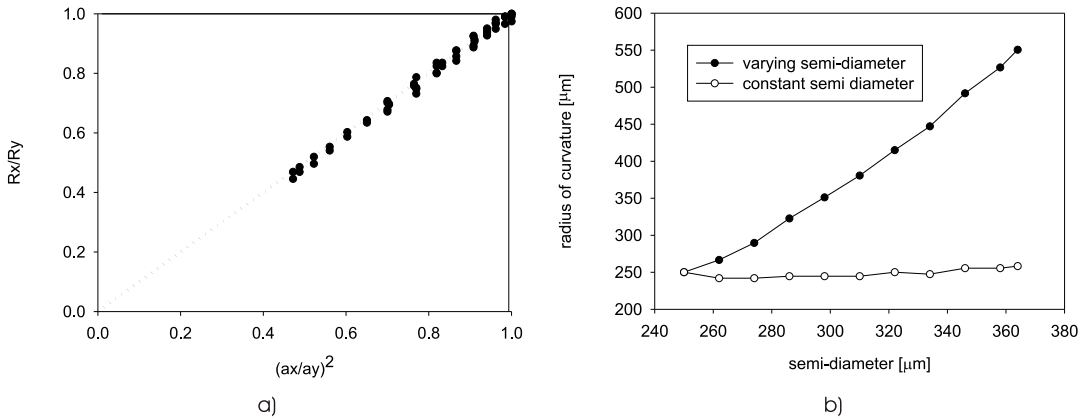

Figure 7. (a): The ratio of radii of curvature R_x/R_y as a function of the ratio of semi–axes $(a_x/a_y)^2$) (Black points are measured values for resist and quartz lenses.). (b): Measured radii of curvature in both axes directions. The size of the short axis remains constant and so does the radius of curvature in this direction. (Measured from resist lenses).

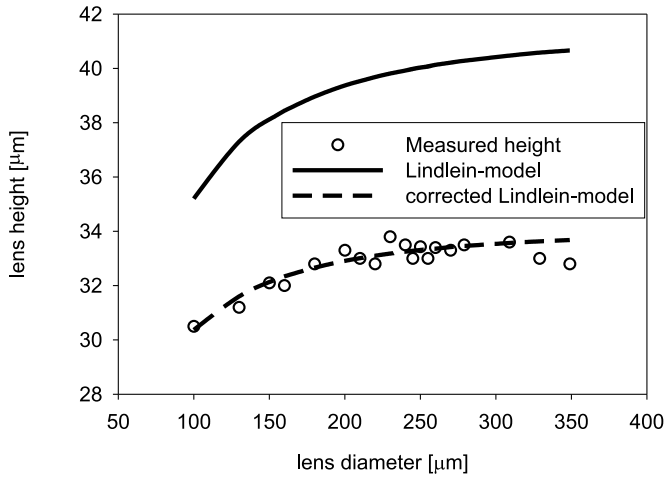

Figure 8. Lens height measured from circular lenses with diameter of 100 to 349 μm on a reflow resist lens wafer. If one corrects for the volume loss, the theoretical curve fits to the measured values.

plotted as dashed line. There is a good agreement for lens diameters smaller than 300 μm at 33 μm lens height. The lens height varies only a few percent for diameters from 200 to 300 μm. At larger diameters than 300 μm the measured values show remarkable differences with the model. This was also seen for the radius of curvature measurements. At fixed lens height and for large semi–diameters (> 300 μm) the radius of curvature becomes too large and doesn't follow anymore the proposed rule. We can state that our design concept for elliptical lenses works well for lenses that are smaller than 300 μm at 33 μm lens height.

3. ARTIFICIAL APPOSITION EYE

3.1. Design

An artificial apposition eye is constructed using a microlens array and a pinhole array in its focal plane. Behind each microlens a small sub–image of the object is generated. Due to a pitch difference between lens array and

pinhole array a magnified moiré image is obtained when the pinholes sample the sub–images. Each channel of this sampling camera corresponds to one field angle in object space – the optical axes of the channels radiate outwards (Fig. 9 a)). The resolution of artificial apposition compound eyes is defined by the interommatidial

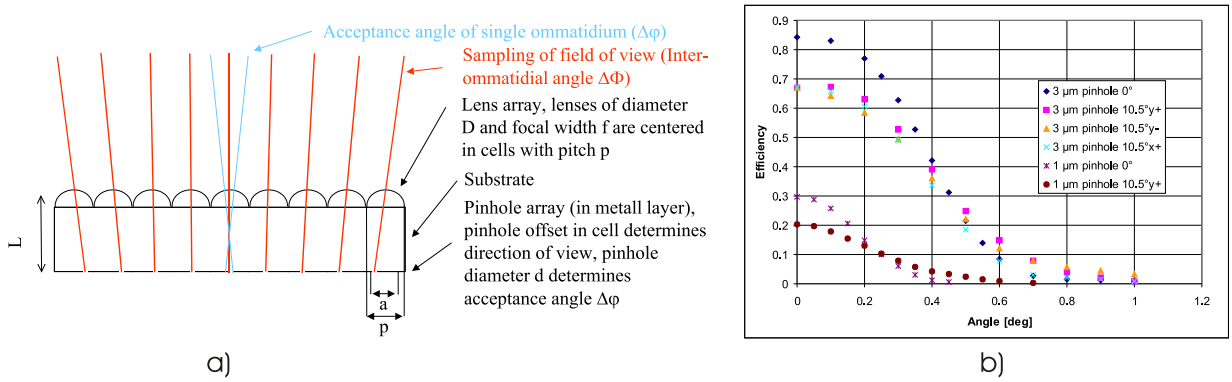

Figure 9. (a): Simplest setup of an artificial apposition compound eye. The optical axes of the ommatidia radiate outwards due to a pitch difference of microlens– and pinhole arrays. (b): Simulated angular sensitivity function for single ommatidium with lens diameter 85 μm and 300 μm focal length in glass. Different pinholes sizes and field angles are examined, the sagittal and the tangential sensitivity functions are given.

angle

$$\Delta\Phi = \arctan\frac{\Delta p}{f}. \tag{2}$$

where Δp is the pitch difference between microlens– and pinhole array and f the focal length of the lenslet and by the acceptance angle of the individual ommatidia

$$\Delta\phi = \arctan\frac{FWHM(d \otimes PSF)}{f} \tag{3}$$

where PSF is the Point Spread Function of a lenslet, d is the aperture function of the pinhole and $\otimes$ stands for convolution. We see that for $FWHM(PSF) \ll FWHM(d)$ the acceptance angle is dominated by the pinhole diameter only and for $FWHM(PSF) \gg FWHM(d)$ the pinhole diameter has minor influence. A reasonable setting would be $FWHM(PSF) \sim FWHM(d)$. The maximum number of resolvable linepairs over the FOV is half the number of channels in the apposition eye if the acceptance angles of the individual ommatidia are perfectly matched (Nyquist criterion). This means that there is no large overlap of the individual FOVs of the different ommatidia. If the acceptance angle of an individual ommatidium is quite large compared to the interommatidial angle the period of resolvable linepairs is determined by the FWHM of the acceptance angle. The FOV of the artificial apposition eye is given by

$$FOV = \arctan\frac{a}{f} \tag{4}$$

where a is the size of the sampled sub–images. We chose $a < p$ in order to maintain some free space between the sub–images to reduce crosstalk and in future to apply baffles which will be described later. In case of $a = p$ the FOV is determined by the NA of the lenslets. The pitch difference of the pinhole array to the lens array for a camera with N channels along one dimension is calculated by

$$\Delta p = a\left(1 - \frac{N}{N+1}\right). \tag{5}$$

The FOV is independently of the number of channels. Due to the extreme short focal length of the imaging system a large depth of field is achieved.

Table 2. Parameters of fabricated artificial apposition eye wafers.

Feature	Parameter	remark / generated by
Metal layer	thickness $200\mu m$	titanium, sputtered
Pinholes	diameter 1–6 μm	photolithography + wet etching
Glass substrate	d = $300\pm1\mu m$	B263T 4 inch wafer
Replicated microlenses	layer thickness $20\mu m$	by UV molding
UV polymer	acrylate type n=1.50	inorganic–organic hybrid polymer
Lens model	$R_c = 118\mu m$, pitch $90\mu m$, dia. 85 μm, sag $10\mu m$	by lithography and reflow
Form deviation	$<$ 20nm RMS	
Size of sampled image	$60\mu m$ x $60\mu m$	gap left to reduce crosstalk
Lateral registration error	$\pm3\mu m$	back side alignment in SUSS Microtec MA6
Axial alignment/ nonuniformity	$\pm6\mu m$ across 4 inch	including focal length nonuniformity
Array sizes	11 x 11 – 101 x 101	each with different pinhole sizes
Viewing angle	21°	on diagonal

A valuable measure of the performance of the single ommatidium is the angular sensitivity function. It predicates which solid angle in object space is treated as one image point by the optical system. Figure 9 b) shows a simulation where the efficiency is normalized to the flux incident on the lens. We see that the apposition eye shows a clear tradeoff between sensitivity and resolution: The larger the pinhole diameter the larger the sensitivity but the worse the resolution (overlap of the individual FOVs) and vice versa. Off–axis aberrations of the outer channels lead to larger spot sizes of image points for larger field angles and thus wider and lower angular sensitivity functions.

The advantages of the artificial apposition eye could especially emerge when used in connection with electronic vision sensors with a very high dynamic range contrast but large pixels with low fill factor.[24] A more detailed analysis of this artificial apposition eye can be found in reference.[25]

3.2. Fabrication

The fabrication of the apposition compound eye has been carried out using lithographical processes on a wafer scale. The approach (as sketched in Fig. 9 a)) is based on the patterning of a thin 4–inch glass wafer with pinhole arrays on one side and microlens arrays on the opposite side. The thickness of the wafer is matched to the microlens focal length. The pitch of the pinholes differs from that of the microlens arrays to realize an individual viewing angle of each channel. The parameters of different arrays on the pinhole photomask (like array size, pinhole pitch and diameter) were varied in such a way, that different camera chips were realized on each wafer. The pinholes (diameters 1 – 6 μm) were generated by photolithography and wet etching of a 200 nm thick metal film on the glass wafer. The generation of the microlens arrays consists of several steps involving master and mold generation and subsequent UV–replication.[26] The photoresist master pattern is fabricated on a silicon wafer in a standard procedure (photolithography in combination with a heating/reflow process). The replication itself is carried out in a modified contact mask aligner (SUSS MA6 with UV embossing option) where the gap between glass wafer and mask/mold is filled by a UV curing inorganic–organic hybrid polymer which is subsequently cured and separated from the mold. The mask aligner enables wedge error compensation as well as lateral and axial alignment of front and back side patterns. The uniformity of the axial distance between lens vertex and pinhole is critical because it is affected by a series of parameters like precision of the MA6 z–axis ($\pm1\mu m$), bowing of the mold, mask holder, chuck, and substrate ($\pm3\mu m$ overall) as well as by nonuniform microlens focal lengths across the wafer ($\pm3\mu m$). A compilation of major technological parameters of the fabricated systems is given in Table 2. In order to investigate the influence of cross talk between channels, we are currently fabricating imaging chips using a modification of the technology. Here, light protection walls shall shield the different channels and thus lead to a reduced crosstalk. The region between pinholes and

microlenses is formed by a laterally patterned spacer layer (thickness $\sim 300\mu m$) consisting of transparent cones of SU8 photopolymer and gaps which are filled by an absorbing polymer cast. High aspect ratio SU8 features are fabricated using an additional photomask. The pinhole and microlens fabrication remains unchanged.

3.3. Experimental Results

For characterization of the presented prototype we registered images of different test objects where the pinhole array surface was imaged on a CCD.

A single mode fiber end face at 637 nm was used as a point source for a measurement of the angular sensitivity function. It was moved laterally in object space at a distance of 300 mm from the lenslet while the power in the pinhole was measured. This power was normalized to the total integrated power of one channel. Figure 10 presents the measured on–axis sensitivity function in case of a 3 μm–pinhole. The measured angular sensitivity

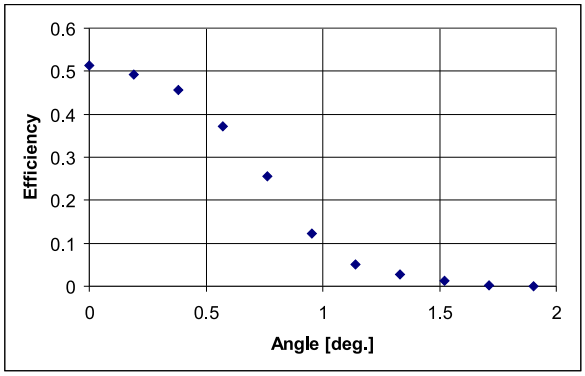

Figure 10. Measured on–axis angular sensitivity function for single ommatidium with lens diameter 85 μm and 300 μm focal length in glass. Pinhole diameter is 3 μm.

function has a FWHM of 1.5° which is almost twice as large as we would have expected from the simulations as presented in Fig. 9 b). Accordingly the experimental efficiency is much lower. From the theoretical sensitivity function in Fig. 9 (FWHM= 0.75°) we would expect that over the horizontal/vertical FOV (15°) approximately 20 linepairs should be resolvable, so that a sampling with 50 x 50 channels would gather all available information.

Figure 11 presents different test images taken by cameras with 101 x 101 channels and relayed by a short working distance–C–mount–objective onto a CCD. The observable distortion and loss of illumination with field angle is due to the relay optics. Images with a high information content can obviously be transferred by the presented artificial apposition compound eye. Larger pinhole diameters result in higher efficiency but lower resolution.

4. CONCLUSIONS AND OUTLOOK

We presented two different artificial compound eye imaging principles. The cluster eye consists of three layers of lenses which form telescope arrays with tilted optical axes. It produces one overall image by annexation of the individual sub–images. The artificial apposition eye consists of a lens array and a pinhole array with different pitch in its focal plane so that the optical axes of the ommatidia radiate outwards. An ommatidium only delivers a signal if a object point is situated on or close to its optical axis. Simulation results for both types of sensors were presented. The experimental examination of elliptical lenses required for aberration correction in the cluster eye was explained. We presented images acquired with the first prototype of an artificial apposition compound eye.

Artificial compound eyes have the capability of a drastic reduction of imaging system length. However the price to be paid is FOV or resolution and sensitivity. Table 3 presents a comparison of the different imaging principles with respect to the major performance criteria.

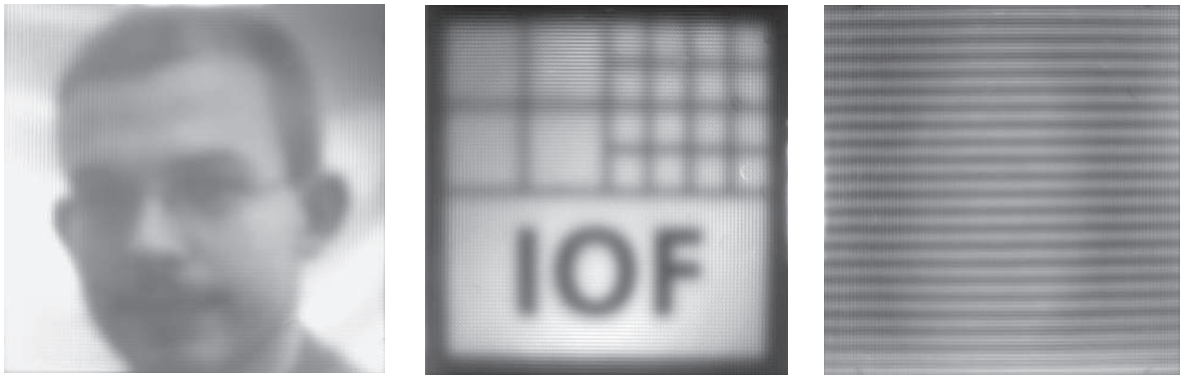

Figure 11. Test patterns imaged by apposition–eye–cameras with 101 x 101 channels. (a): Image of a passport photograph of the principal author (pinhole diameter 4 μm). (b): Image of the institute–logo (pinhole diameter 3 μm). (c): Image of a test target with 22 linepairs over the horizontal/vertical FOV which corresponds to a resolution of 1.5 lp/deg. (pinhole diameter 3 μm). Test objects fill the FOV of the camera under test. The object distance has no influence on the image quality.

Table 3. Comparison of different imaging principles and parameters that define or limit the optical performance.

Type	**Single aperture eye**	**Cluster eye**	**Apposition eye**
Possible $F/\#$	low	high	low
Image formation	One overall image (classical principle)	One overall image (optical annexation)	Pattern of illuminated pinholes
Possible length for 4.5 mm image circle	$\geq$ 4 mm	0.5 – 3 mm	0.05 – 1 mm
Magnification	low Focal length of lens	high Ratio of focal lengths of telescope	low Focal length of lenslet
Resolution	high(diffr. limited)	low(aberrations)	low (space–bandwidth–product)
Sensitivity	high	low	high (size of pinholes)
FOV	Focal length and detector diagonal	Lateral offset of lenses and magnification	$F/\#$ (if image size $\approx$ lens size)

Future work on the two presented imaging principles will include the lithographic construction of light protection walls using absorbing polymer to reduce crosstalk of the artificial apposition eye. The mask generation for the different layers of lenses and apertures of a first cluster eye is underway.

ACKNOWLEDGMENTS

This work was funded by the European Commission, Project No.: IST-2001-34646, WALORI - WAfer Level Optic solution foR compact CMOS Imager. We greatfully acknowledge for the preparation of the mask for the examination of elliptical lenses by M. Flury (now at University of St. Etienne, France) and for the fabrication of microlens– and pinhole arrays for the artificial apposition eye by G. Wagener, S. Kleinle and A. Oelschläger (Fraunhofer–Institut für Angewandte Optik und Feinmechanik).

REFERENCES

1. A. W. Lohmann, "Scaling laws for lens systems," *Appl. Opt.* **28**, pp. 4996–4998, December 1989.

2. R. Völkel, M. Eisner, and K. J. Weible, "Miniaturized imaging systems," in *Micro- and Nanoengineering, International Conference*, (Lugano, Switzerland), September 2002.
3. M. F. Land, "The optics of animal eyes," *Contemporary Physics* **29**, pp. 435–455, September/October 1988.
4. G. A. Horridge, "The compound eye of insects," *Scientific American* **237**, pp. 108–120, July 1977.
5. A. W. Snyder, "Acuity of compound eyes: Physical limitations and design," *Journal of Comparative Physiology A* **116**, pp. 161–182, 1977.
6. K. Kirschfeld, "The absolute sensitivity of lens and compound eyes," *Zeitschrift für Naturforschung* **29**, pp. 592–596, 1974.
7. R. Wehner, "Spatial vision in arthropods," in *Comparative Physiology and Evolution of Vision in Invertebrates - Handbook of Sensory Physiology*, H. Autrum, ed., **VII/6C**, ch. 4, pp. 287–317, 551–616, Springer Verlag, Berlin-Heidelberg, 1981.
8. J. S. Sanders and C. E. Halford, "Design and analysis of apposition compound eye optical sensors," *Opt. Eng.* **34**, pp. 222–235, January 95.
9. M. F. Land, "Variations in structure and design of compound eyes," in *Facets of Vision*, D. Stavenga and R. C. Hardie, eds., ch. 5, pp. 90–111, Springer Verlag, 1989.
10. G. A. Horridge, "Apposition eyes of large diurnal insects as organs adapted to seeing," *Proceedings of the Royal Society of London B* **207**, pp. 287–309, 1980.
11. K. Hamanaka and H. Koshi, "An artificial compound eye using a microlens array and its application to scale-invariant processing," *Optical Review* **3**(4), pp. 264–268, 1996.
12. S. Ogata, J. Ishida, and T. Sasano, "Optical sensor array in an artificial compound eye," *Opt. Eng.* **33**, pp. 3649–3655, November 1994.
13. J. Tanida, T. Kumagai, K. Yamada, and S. Miyatake, "Thin observation module by bound optics (tombo) concept and experimental verification," *Appl. Opt.* **40**, pp. 1806–1813, April 2001.
14. M. F. Land, F. A. Burton, and V. B. M. Rochow, "The optical geometry of euphausiid eyes," *Journal of Comparative Physiology A* **130**(1), pp. 49–62, 1979.
15. D. Gabor, "Improvements in or relating to optical systems composed of lenticules," *Patent Specification* **UK 541 753**, December 1940.
16. C. Hembd, R. Stevens, and M. Hutley, "Imaging properties of the "Gabor Superlens"," in *Microlens Arrays, EOS Topical Meeting, National Physical Laboratory*, (Teddington, UK), May 1997.
17. S. Wallstab and R. Völkel, "Flachbauendes Bilderfassungssystem," *Offenlegungsschrift* **DE 199 17 890 A1**, November 2000.
18. N. Lindlein, "Simulation of micro-optical systems including microlens arrays," *J. Opt. A: Pure Appl. Opt.* **4**, pp. 1–9, 2002.
19. A. E. Siegmann, *Lasers*, Mill Valey, CA: University Science, 1986.
20. J. Duparré, P. Schreiber, and R. Völkel, "Theoretical analysis of an artificial superposition compound eye for application in ultra flat digital image acquisition devices," in *Optical systems design*, *Proc. SPIE 5249* , SPIE, (St. Etienne, France), September 2003.
21. H. Naumann and G. Schröder, *Bauelemente der Optik - Taschenbuch der technischen Optik*, Hanser Verlag, München, Wien, 6 ed., 1992.
22. R. McCluney, *Introduction to Radiometry and Photometry*, Artech House, Boston, London, 1994.
23. N. Lindlein, S. Haselbeck, and J. Schwider, "Simplified theory for ellipsoidal melted microlenses," in *Microlens Arrays*, *EOS Topical Meetings Digest Series, Vol. 5* , EOS, (Teddington, UK), May 1995.
24. P.-F. Rüedi, P. Heim, F. Kaess, E. Grenet, F. Heitger, P.-Y. Burgi, S. Gyger, and P. Nussbaum, "A 128 x 128 pixel 120dB dynamic range vision sensor chip for image contrast and orientation extraction," in *IEEE International Solid-State Circuits Conference*, *Digest of Technical Papers* , p. Paper 12.8, IEEE, February 2003.
25. J. Duparré, P. Dannberg, P. Schreiber, and A. Bräuer, "Micro–optically fabricated artificial apposition compound eye," in *Electronic Imaging - Science and Technology*, *Proc. SPIE 5301* , IS&T/SPIE, (San Jose, USA), January 2004.
26. P. Dannberg, G. Mann, L. Wagner, and A. Bräuer, "Polymer UV-molding for micro-optical systems and O/E-integration," *Proc. SPIE 4179* , p. 137 ff, SPIE, 2000.